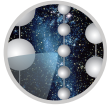


2 In-situ calibration of the single-photoelectron charge 3 response of the IceCube photomultiplier tubes



4 ICECUBE

5 IceCube collaboration

6 M. G. Aartsen,^p M. Ackermann,^{bc} J. Adams,^p J. A. Aguilar,^l M. Ahlers,^t M. Ahrens,^{at}
7 C. Alispach,^z K. Andeen,^{ak} T. Anderson,^{az} I. Ansseau,^l G. Anton,^x C. Argüelles,ⁿ
8 J. Auffenberg,^a S. Axani,ⁿ P. Backes,^a H. Bagherpour,^p X. Bai,^{aq} A. Balagopal V.,^{ac}
9 A. Barbano,^z S. W. Barwick,^{ab} B. Bastian,^{bc} V. Baum,^{aj} S. Baur,^l R. Bay,^h J. J. Beatty,^{r,s}
10 K.-H. Becker,^{bb} J. Becker Tjus,^k S. BenZvi,^{as} D. Berley,^q E. Bernardini,^{bc,bd}
11 D. Z. Besson,^{ad,be} G. Binder,^{h,i} D. Bindig,^{bb} E. Blaufuss,^q S. Blot,^{bc} C. Boehm,^{at} M. Börner,^u
12 S. Böser,^{aj} O. Botner,^{ba} J. Böttcher,^a E. Bourbeau,^t J. Bourbeau,^{ai} F. Bradascio,^{bc}
13 J. Braun,^{ai} S. Bron,^z J. Brostean-Kaiser,^{bc} A. Burgman,^{ba} J. Buscher,^a R. S. Busse,^{al}
14 T. Carver,^z C. Chen,^f E. Cheung,^q D. Chirkin,^{ai} S. Choi,^{av} K. Clark,^{ae} L. Classen,^{al}
15 A. Coleman,^{am} G. H. Collin,ⁿ J. M. Conrad,ⁿ P. Coppin,^m P. Correa,^m D. F. Cowen,^{ay,az}
16 R. Cross,^{as} P. Dave,^f C. De Clercq,^m J. J. DeLaunay,^{az} H. Dembinski,^{am} K. Deoskar,^{at}
17 S. De Ridder,^{aa} P. Desiati,^{ai} K. D. de Vries,^m G. de Wasseige,^m M. de With,^j T. DeYoung,^v
18 A. Diaz,ⁿ J. C. Díaz-Vélez,^{ai} H. Dujmovic,^{av} M. Dunkman,^{az} E. Dvorak,^{aq} B. Eberhardt,^{ai}
19 T. Ehrhardt,^{aj} P. Eller,^{az} R. Engel,^{ac} P. A. Evenson,^{am} S. Fahey,^{ai} A. R. Fazely,^g J. Felde,^q
20 K. Filimonov,^h C. Finley,^{at} D. Fox,^{ay} A. Franckowiak,^{bc} E. Friedman,^q A. Fritz,^{aj}
21 T. K. Gaisser,^{am} J. Gallagher,^{ah} E. Ganster,^a S. Garrappa,^{bc} L. Gerhardt,ⁱ K. Ghorbani,^{ai}
22 T. Glauch,^y T. Glüsenkamp,^x A. Goldschmidt,ⁱ J. G. Gonzalez,^{am} D. Grant,^v Z. Griffith,^{ai}
23 S. Griswold,^{as} M. Günder,^a M. Gündüz,^k C. Haack,^a A. Hallgren,^{ba} L. Halve,^a F. Halzen,^{ai}
24 K. Hanson,^{ai} A. Haungs,^{ac} D. Hebecker,^j D. Heereman,^l P. Heix,^a K. Helbing,^{bb} R. Hellauer,^q
25 F. Henningsen,^y S. Hickford,^{bb} J. Hignight,^w G. C. Hill,^b K. D. Hoffman,^q R. Hoffmann,^{bb}
26 T. Hoinka,^u B. Hokanson-Fasig,^{ai} K. Hoshina,^{ai,be} F. Huang,^{az} M. Huber,^y T. Huber,^{ac,bc}
27 K. Hultqvist,^{at} M. Hünnefeld,^u R. Hussain,^{ai} S. In,^{av} N. Iovine,^l A. Ishihara,^o G. S. Japaridze,^e
28 M. Jeong,^{av} K. Jero,^{ai} B. J. P. Jones,^d F. Jonske,^a R. Joppe,^a D. Kang,^{ac} W. Kang,^{av}
29 A. Kappes,^{al} D. Kappesser,^{aj} T. Karg,^{bc} M. Karl,^y A. Karle,^{ai} U. Katz,^x M. Kauer,^{ai}
30 J. L. Kelley,^{ai} A. Kheirandish,^{ai} J. Kim,^{av} T. Kintscher,^{bc} J. Kiryluk,^{au} T. Kittler,^x
31 S. R. Klein,^{h,i} R. Koirala,^{am} H. Kolanoski,^j L. Köpke,^{aj} C. Kopper,^v S. Kopper,^{ax}
32 D. J. Koskinen,^t M. Kowalski,^{j,bc} K. Krings,^y G. Krückl,^{aj} N. Kulacz,^w N. Kurahashi,^{ap}
33 A. Kyriacou,^b M. Labare,^{aa} J. L. Lanfranchi,^{az} M. J. Larson,^q F. Lauber,^{bb} J. P. Lazar,^{ai}
34 K. Leonard,^{ai} A. Leszczyńska,^{ac} M. Leuermann,^a Q. R. Liu,^{ai} E. Lohfink,^{aj}

35 C. J. Lozano Mariscal,^{al} L. Lu,^o F. Lucarelli,^z J. Lünemann,^m W. Luszczak,^{ai} Y. Lyu,^{h,i}
 36 W. Y. Ma,^{bc} J. Madsen,^{ar} G. Maggi,^m K. B. M. Mahn,^v Y. Makino,^o P. Mallik,^a K. Mallot,^{ai}
 37 S. Mancina,^{ai} I. C. Mariş,^l R. Maruyama,^{an} K. Mase,^o R. Maunu,^q F. McNally,^{ag} K. Meagher,^{ai}
 38 M. Medici,^t A. Medina,^s M. Meier,^u S. Meighen-Berger,^y T. Menne,^u G. Merino,^{ai} T. Meures,^l
 39 J. Micallef,^v D. Mockler,^l G. Momenté,^{aj} T. Montaruli,^z R. W. Moore,^w R. Morse,^{ai} M. Moulai,ⁿ
 40 P. Muth,^a R. Nagai,^o U. Naumann,^{bb} G. Neer,^v H. Niederhausen,^y M. U. Nisa,^v S. C. Nowicki,^v
 41 D. R. Nygren,ⁱ A. Obertacke Pollmann,^{bb} M. Oehler,^{ac} A. Olivas,^q A. O’Murchadha,^l
 42 E. O’Sullivan,^{at} T. Palczewski,^{h,i} H. Pandya,^{am} D. V. Pankova,^{az} N. Park,^{ai} P. Peiffer,^{aj}
 43 C. Pérez de los Heros,^{ba} S. Philippen,^a D. Pieloth,^u E. Pinat,^l A. Pizzuto,^{ai} M. Plum,^{ak}
 44 A. Porcelli,^{aa} P. B. Price,^h G. T. Przybylski,ⁱ C. Raab,^l A. Raissi,^p M. Rameez,^t L. Rauch,^{bc}
 45 K. Rawlins,^c I. C. Rea,^y R. Reimann,^a B. Relethford,^{ap} M. Renschler,^{ac} G. Renzi,^l
 46 E. Resconi,^y W. Rhode,^u M. Richman,^{ap} S. Robertson,ⁱ M. Rongen,^a C. Rott,^{av} T. Ruhe,^u
 47 D. Ryckbosch,^{aa} D. Rysewyk,^v I. Safa,^{ai} S. E. Sanchez Herrera,^v A. Sandrock,^u
 48 J. Sandros,^{aj} M. Santander,^{ax} S. Sarkar,^{ao} S. Sarkar,^w K. Satalecka,^{bc} M. Schaufel,^a
 49 H. Schieler,^{ac} P. Schlunder,^u T. Schmidt,^q A. Schneider,^{ai} J. Schneider,^x
 50 F. G. Schröder,^{ac,am} L. Schumacher,^a S. Sclafani,^{ap} D. Seckel,^{am} S. Seunarine,^{ar}
 51 S. Shefali,^a M. Silva,^{ai} R. Snihur,^{ai} J. Soedingrekso,^u D. Soldin,^{am} M. Song,^q
 52 G. M. Spiczak,^{ar} C. Spiering,^{bc} J. Stachurska,^{bc} M. Stamatikos,^s T. Stanev,^{am} R. Stein,^{bc}
 53 P. Steinmüller,^{ac} J. Stettner,^a A. Steuer,^{aj} T. Stezelberger,ⁱ R. G. Stokstad,ⁱ A. Stöbl,^o
 54 N. L. Strotjohann,^{bc} T. Stürwald,^a T. Stuttard,^t G. W. Sullivan,^q I. Taboada,^f F. Tenholt,^k
 55 S. Ter-Antonyan,^g A. Terliuk,^{bc} S. Tilav,^{am} K. Tollefson,^v L. Tomankova,^k C. Tönnis,^{aw}
 56 S. Toscano,^l D. Tosi,^{ai} A. Trettin,^{bc} M. Tselengidou,^x C. F. Tung,^f A. Turcati,^y R. Turcotte,^{ac}
 57 C. F. Turley,^{az} B. Ty,^{ai} E. Unger,^{ba} M. A. Unland Elorrieta,^{al} M. Usner,^{bc} J. Vandenbroucke,^{ai}
 58 W. Van Driessche,^{aa} D. van Eijk,^{ai} N. van Eijndhoven,^m S. Vanheule,^{aa} J. van Santen,^{bc}
 59 M. Vraeghe,^{aa} C. Walck,^{at} A. Wallace,^b M. Wallraff,^a N. Wandkowsky,^{ai} T. B. Watson,^d
 60 C. Weaver,^w A. Weindl,^{ac} M. J. Weiss,^{az} J. Weldert,^{aj} C. Wendt,^{ai} J. Werthebach,^{ai}
 61 B. J. Whelan,^b N. Whitehorn,^{af} K. Wiebe,^{aj} C. H. Wiebusch,^a L. Wille,^{ai} D. R. Williams,^{ax}
 62 L. Wills,^{ap} M. Wolf,^y J. Wood,^{ai} T. R. Wood,^w K. Woschnagg,^h G. Wrede,^x D. L. Xu,^{ai}
 63 X. W. Xu,^g Y. Xu,^{au} J. P. Yanez,^w G. Yodh,^{ab} S. Yoshida,^o T. Yuan^{ai} and M. Zöcklein^a

64 ^a*III. Physikalisches Institut, RWTH Aachen University, D-52056 Aachen, Germany*

65 ^b*Department of Physics, University of Adelaide, Adelaide, 5005, Australia*

66 ^c*Dept. of Physics and Astronomy, University of Alaska Anchorage, 3211 Providence Dr., Anchorage, AK*
 67 *99508, USA*

68 ^d*Dept. of Physics, University of Texas at Arlington, 502 Yates St., Science Hall Rm 108, Box 19059,*
 69 *Arlington, TX 76019, USA*

70 ^e*CTSPS, Clark-Atlanta University, Atlanta, GA 30314, USA*

71 ^f*School of Physics and Center for Relativistic Astrophysics, Georgia Institute of Technology, Atlanta, GA*
 72 *30332, USA*

73 ^g*Dept. of Physics, Southern University, Baton Rouge, LA 70813, USA*

74 ^h*Dept. of Physics, University of California, Berkeley, CA 94720, USA*

75 ⁱ*Lawrence Berkeley National Laboratory, Berkeley, CA 94720, USA*

76 ^j*Institut für Physik, Humboldt-Universität zu Berlin, D-12489 Berlin, Germany*

77 ^k*Fakultät für Physik & Astronomie, Ruhr-Universität Bochum, D-44780 Bochum, Germany*

78 ^l *Université Libre de Bruxelles, Science Faculty CP230, B-1050 Brussels, Belgium*
79 ^m *Vrije Universiteit Brussel (VUB), Dienst ELEM, B-1050 Brussels, Belgium*
80 ⁿ *Dept. of Physics, Massachusetts Institute of Technology, Cambridge, MA 02139, USA*
81 ^o *Dept. of Physics and Institute for Global Prominent Research, Chiba University, Chiba 263-8522, Japan*
82 ^p *Dept. of Physics and Astronomy, University of Canterbury, Private Bag 4800, Christchurch, New Zealand*
83 ^q *Dept. of Physics, University of Maryland, College Park, MD 20742, USA*
84 ^r *Dept. of Astronomy, Ohio State University, Columbus, OH 43210, USA*
85 ^s *Dept. of Physics and Center for Cosmology and Astro-Particle Physics, Ohio State University, Columbus,*
86 *OH 43210, USA*
87 ^t *Niels Bohr Institute, University of Copenhagen, DK-2100 Copenhagen, Denmark*
88 ^u *Dept. of Physics, TU Dortmund University, D-44221 Dortmund, Germany*
89 ^v *Dept. of Physics and Astronomy, Michigan State University, East Lansing, MI 48824, USA*
90 ^w *Dept. of Physics, University of Alberta, Edmonton, Alberta, Canada T6G 2E1*
91 ^x *Erlangen Centre for Astroparticle Physics, Friedrich-Alexander-Universität Erlangen-Nürnberg, D-91058*
92 *Erlangen, Germany*
93 ^y *Physik-department, Technische Universität München, D-85748 Garching, Germany*
94 ^z *Département de physique nucléaire et corpusculaire, Université de Genève, CH-1211 Genève, Switzerland*
95 ^{aa} *Dept. of Physics and Astronomy, University of Gent, B-9000 Gent, Belgium*
96 ^{ab} *Dept. of Physics and Astronomy, University of California, Irvine, CA 92697, USA*
97 ^{ac} *Karlsruhe Institute of Technology, Institut für Kernphysik, D-76021 Karlsruhe, Germany*
98 ^{ad} *Dept. of Physics and Astronomy, University of Kansas, Lawrence, KS 66045, USA*
99 ^{ae} *SNOLAB, 1039 Regional Road 24, Creighton Mine 9, Lively, ON, Canada P3Y 1N2*
100 ^{af} *Department of Physics and Astronomy, UCLA, Los Angeles, CA 90095, USA*
101 ^{ag} *Department of Physics, Mercer University, Macon, GA 31207-0001, USA*
102 ^{ah} *Dept. of Astronomy, University of Wisconsin, Madison, WI 53706, USA*
103 ^{ai} *Dept. of Physics and Wisconsin IceCube Particle Astrophysics Center, University of Wisconsin, Madison,*
104 *WI 53706, USA*
105 ^{aj} *Institute of Physics, University of Mainz, Staudinger Weg 7, D-55099 Mainz, Germany*
106 ^{ak} *Department of Physics, Marquette University, Milwaukee, WI, 53201, USA*
107 ^{al} *Institut für Kernphysik, Westfälische Wilhelms-Universität Münster, D-48149 Münster, Germany*
108 ^{am} *Bartol Research Institute and Dept. of Physics and Astronomy, University of Delaware, Newark, DE 19716,*
109 *USA*
110 ^{an} *Dept. of Physics, Yale University, New Haven, CT 06520, USA*
111 ^{ao} *Dept. of Physics, University of Oxford, Parks Road, Oxford OX1 3PU, UK*
112 ^{ap} *Dept. of Physics, Drexel University, 3141 Chestnut Street, Philadelphia, PA 19104, USA*
113 ^{aq} *Physics Department, South Dakota School of Mines and Technology, Rapid City, SD 57701, USA*
114 ^{ar} *Dept. of Physics, University of Wisconsin, River Falls, WI 54022, USA*
115 ^{as} *Dept. of Physics and Astronomy, University of Rochester, Rochester, NY 14627, USA*
116 ^{at} *Oskar Klein Centre and Dept. of Physics, Stockholm University, SE-10691 Stockholm, Sweden*
117 ^{au} *Dept. of Physics and Astronomy, Stony Brook University, Stony Brook, NY 11794-3800, USA*
118 ^{av} *Dept. of Physics, Sungkyunkwan University, Suwon 16419, Korea*
119 ^{aw} *Institute of Basic Science, Sungkyunkwan University, Suwon 16419, Korea*
120 ^{ax} *Dept. of Physics and Astronomy, University of Alabama, Tuscaloosa, AL 35487, USA*
121 ^{ay} *Dept. of Astronomy and Astrophysics, Pennsylvania State University, University Park, PA 16802, USA*

122 ^{az}*Dept. of Physics, Pennsylvania State University, University Park, PA 16802, USA*

123 ^{ba}*Dept. of Physics and Astronomy, Uppsala University, Box 516, S-75120 Uppsala, Sweden*

124 ^{bb}*Dept. of Physics, University of Wuppertal, D-42119 Wuppertal, Germany*

125 ^{bc}*DESY, D-15738 Zeuthen, Germany*

126 ^{bd}*also at Università di Padova, I-35131 Padova, Italy*

127 ^{be}*also at National Research Nuclear University, Moscow Engineering Physics Institute (MEPhI), Moscow*
128 *115409, Russia*

129 ^{bf}*Earthquake Research Institute, University of Tokyo, Bunkyo, Tokyo 113-0032, Japan*

130 *E-mail: analysis@icecube.wisc.edu*

131 **ABSTRACT:** We describe an improved in-situ calibration of the single-photoelectron charge distri-
132 **butions** for each of the in-ice Hamamatsu Photonics R7081-02[MOD] photomultiplier tubes in
133 **the IceCube Neutrino Observatory.** The accurate characterization of the individual PMT charge
134 **distributions** is important for PMT calibration, data and Monte Carlo simulation agreement, and
135 **understanding** the effect of hardware differences within the detector. We discuss the single photo-
136 **electron identification** procedure and how we extract the single-photoelectron charge distribution
137 **using a deconvolution** of the multiple-photoelectron charge distribution.

138 **KEYWORDS:** IceCube, single-photoelectron charge distribution, photomultiplier tubes, calibration

139 **ARXIV EPRINT:** [tbd](#)

140 **Contents**

| | | |
|-----|--|-----------|
| 141 | 1 Introduction | 1 |
| 142 | 1.1 Single-photoelectron charge distributions | 3 |
| 143 | 1.2 IceCube datasets and software definitions | 5 |
| 144 | 2 Extracting the SPE charge templates | 6 |
| 145 | 2.1 Single photoelectron pulse selection | 6 |
| 146 | 2.2 Characterizing the low-charge region | 8 |
| 147 | 2.3 Fitting procedure | 9 |
| 148 | 2.4 SPE charge template fit results | 10 |
| 149 | 3 Discussion | 11 |
| 150 | 3.1 Correlations between fit parameters and DOM hardware differences | 11 |
| 151 | 3.2 Fitting parameters variation over time | 12 |
| 152 | 3.3 Quantifying observable changes when modifying the PMT charge distributions | 13 |
| 153 | 3.3.1 Model comparison | 15 |
| 154 | 3.4 SPE charge templates for calibration | 15 |
| 155 | 3.5 SPE charge templates in simulation | 15 |
| 156 | 4 Conclusion | 16 |

157 **1 Introduction**

158 The IceCube Neutrino Observatory [1, 2] is a cubic-kilometer-sized array of 5,160 photomultiplier
159 tubes (PMTs) buried in the Antarctic ice sheet, designed to observe high-energy neutrinos interacting
160 with the ice [3]. In 2011, the IceCube Collaboration completed the installation of 86 vertical *strings*
161 of PMT modules, eight of which were arranged in a denser configuration known as the DeepCore
162 sub-array [4]. Each string in IceCube contains 60 digital optical modules (DOMs), which contain
163 a single PMT each, as well as all required electronics [5]. The primary 78 strings (excluding
164 DeepCore) are spaced 125 m apart in a hexagonal grid, with the DOMs extending from 1450 m to
165 2450 m below the surface of the ice sheet. The additional DeepCore strings (79-86) are positioned
166 between the centermost strings in the detector, reducing the horizontal DOM-to-DOM distance in
167 this region to 42 m and 72 m. The lower 50 DOMs on these strings are located in the deepest 350 m
168 of the detector near the clearest ice, while the upper ten provide a cosmic ray veto extending down
169 from 1900 m to 2000 m below the surface.

170 Each DOM consists of a 0.5"-thick spherical glass pressure vessel that houses a single down-
171 facing 10" PMT from Hamamatsu Photonics. The PMT is coupled to the glass housing with optical
172 gel and is surrounded by a wire mesh of mu metal to reduce the effect of the Earth's ambient
173 magnetic field. The glass housing is transparent to wavelengths 350 nm and above [6].

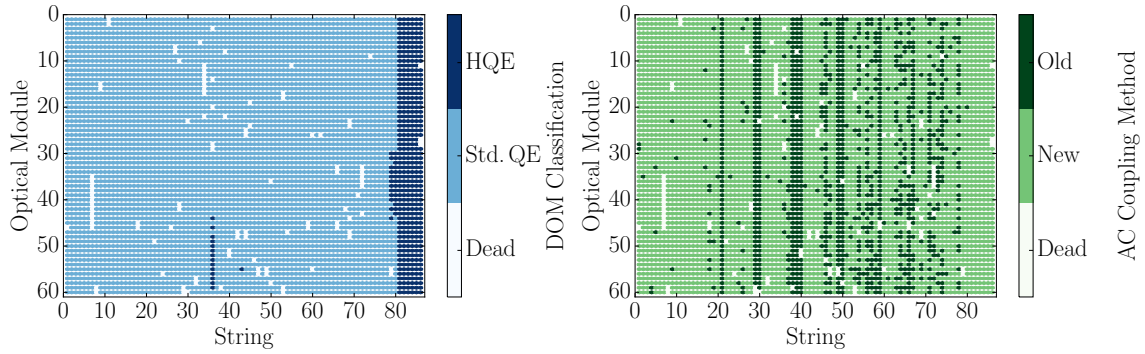


Figure 1. Left: A mapping of the HQE (dark blue) and Standard QE DOMs (light blue). Right: The version of AC coupling, old toroids (dark green) and new toroids (light green). DOMs that have been removed from service are shown in white.

174 Of the 5,160 DOMs, 4,762 house a R7081-02 Hamamatsu Photonics PMT, sensitive to wave-
 175 lengths ranging from 300 nm to 650 nm, with peak quantum efficiency of 25% near 390 nm. These
 176 are classified as Standard Quantum Efficiency (Standard QE) DOMs. The remaining 398 DOMs
 177 are equipped with the Hamamatsu R7081-02MOD PMTs, which, having a peak quantum efficiency
 178 of 34% near 390 nm (36% higher efficiency than the Standard QE DOMs), are classified as High
 179 Quantum Efficiency (HQE) DOMs [4]. These DOMs are primarily located in DeepCore and on
 180 strings 36 and 43, as shown in the left side of Fig. 1.

181 The R7081-02 and R7081-02MOD PMTs have 10 dynode stages and are operated with a
 182 nominal gain of 10^7 and high voltage ranging from approximately 1215 ± 83 V and 1309 ± 72 V,
 183 respectively. A typical amplified single photoelectron generates a 5.2 ± 0.3 mV peak voltage after
 184 digitization with a full width half maximum of 13 ± 1 ns. The PMTs operate with the anodes at
 185 high voltage, so the signal is AC-coupled to the front-end amplifiers. There are two versions of AC
 186 coupling in the detectors, referred to as the *new* and *old toroids*, both of which use custom-designed
 187 wideband bifilar wound 1:1 toroidal transformers¹. The locations of DOMs with the different
 188 versions of AC-coupling are shown on the right side of Fig. 1. The DOMs with the old toroids
 189 were designed with an impedance of 43Ω , while the new toroids are 50Ω [7]. All HQE DOMs are
 190 instrumented with the new toroids.

191 IceCube relies on two observables per DOM to reconstruct events: the total number of detected
 192 photons and their timing distribution. Both the timing and the number of photons are extracted from
 193 the digitized waveforms. This is accomplished by deconvolving the waveforms [8] into a series of
 194 scaled single photoelectron pulses (so-called pulse series), and the integral of the individual pulses
 195 (divided by the load resistance) defines the observed charge. It will often be expressed in units of
 196 PE, or photoelectrons, which further divides the measured charge by the charge of a single electron
 197 times the nominal gain.

198 When one or more photons produce a voltage at the anode sufficient to trigger the onboard

¹The toroidal transformer effectively acts as a high-pass filter with good signal fidelity at high frequencies and offers a higher level of reliability than capacitive coupling. Conventional AC-coupling high-voltage ceramic capacitors can also produce undesirable noise from leakage currents and are impractical given the signal droop and undershoot requirements [6].

199 discriminator (set via a DAC to approximately 1.2 mV, or equivalently to ~ 0.23 PE), the signal
200 acquisition process is triggered. The signal is fed into four parallel channels for digitization. Three
201 channels pass through a 75 ns delay loop in order to capture the leading edge of the triggering pulse,
202 and are then subject to different levels of amplification prior to being digitized by a high-speed
203 (300 MSPS for 128 samples) 10-bit Analog Transient Waveform Digitizer (ATWD). The high-gain
204 channel has a nominal amplification of 16 and is most suitable for single photon detection. Two
205 ATWD chips are present on the DOM Mainboard (MB) and operate in a ping-pong fashion to
206 remove dead time associated with the readout. The signal to the fourth parallel channel is first
207 shaped and amplified, then fed into a 10-bit fast analog-to-digital converter (fADC) operating at a
208 sampling rate of 40 MSPS. Further detail regarding the description of the DOM electronics can be
209 found in Refs. [5, 9].

210 This article discusses an accurate method for determining the in-situ individual PMT single-
211 photoelectron charge distributions, which can be used to improve calibration and the overall detector
212 description in Monte Carlo (MC) simulation. The SPE charge distribution refers to the charge
213 probability density function of an individual PMT generated by the amplification of a pure sample
214 of single photoelectrons. The measured shape of the SPE charge distributions is shown to be useful
215 for examining hardware differences and long term stability of the detector. This was recently made
216 possible with the development of two pieces of software:

- 217 1. A specially-designed unbiased pulse selection developed to reduce the multiple photoelec-
218 tron (MPE) contamination while accounting for other physical phenomena (e.g. late pulses,
219 afterpulses, pre-pulses, and baseline shifts) and software-related effects (e.g. pulse splitting).
220 This is further described in Sec. 2.1.
- 221 2. A fitting procedure developed to separate the remaining MPE contamination from the SPE
222 charge distribution by deconvolving the measured charged distribution. This is further de-
223 scribed in Sec. 2.3.

224 By using in-situ data to determine the SPE charge distributions, we accurately represent the
225 individual PMT response as a function of time, environmental conditions, software version and
226 hardware differences, and realistic photocathode illumination conditions. This is beneficial since
227 it also allows us to inspect the stability and long-term behavior of the individual DOMs, verify
228 previous calibration, and correlate features with specific DOM hardware.

229 1.1 Single-photoelectron charge distributions

230 Ideally, a single photon produces a single photoelectron, which is then amplified by a known
231 amount, and the measured charge corresponds to 1 PE. However, there are many physical processes
232 that create structure in the measured charge distributions. For example:

- 233 • **Statistical fluctuation due to cascade multiplication** [10]. At every stage of dynode
234 amplification, there is a stochastic spread in the number of emitted electrons that make it to
235 the next dynode. This in turn causes a spread in the measured charge after the gain stage of
236 the PMT.

- 237 • **Photoelectron trajectory.** Some electrons may deviate from the favorable trajectory, re-
 238 ducing the number of secondaries produced at a dynode or the efficiency to collect them
 239 on the following dynode. This can occur at any stage, but it has the largest effect on the
 240 multiplication at the first dynode [11]. The trajectory of a photoelectron striking the first
 241 dynode will depend on many things, including where on the photocathode it was emitted,
 242 the uniformity of the electric field, the size and shape of the dynodes [10], and the ambient
 243 magnetic field [12, 13].

- 244 • **Late or delayed pulses.** A photoelectron can elastically or inelastically scatter off the first
 245 dynode. The scattered electron can then be re-accelerated to the dynode, creating a second
 246 pulse. The difference in time between the initial pulse and the re-accelerated pulse in the
 247 R7081-02 PMT was previously measured to be up to 70 ns [6, 14]. The two sub-pulses have
 248 lower charges, but the sum of the two tends to add up to the original charge. Collecting either
 249 the initial pulse or the late pulse will result in the charge being reconstructed in the low-PE
 250 region [15].

- 251 • **Afterpulses.** When photoelectrons or the secondary electrons produced during the electron
 252 cascade gain sufficient energy to ionize residual gas in the PMT, the positively charged ionized
 253 gas will be accelerated in the electric field towards the photocathode. Upon impact with the
 254 photocathode, electrons can be released from the photocathode, creating what is called an
 255 afterpulse. For the R7081-02 PMTs, the timescale for afterpulses was measured to occur
 256 from 0.3 to 11 μ s after the initial pulse, with the first prominent afterpulse peak occurring
 257 at approximately 600 ns [6]. The spread in the afterpulse time depends on the position
 258 of photocathode, the charge-to-mass ratio of the ion produced, and the electric potential
 259 distribution [16], whereas the size of the afterpulse is related to the momentum and species
 260 of the ionized gas and composition of the photocathode [17].

- 261 • **Pre-pulses.** If an incident photon passes through the photocathode without interaction and
 262 strikes one of the dynodes, it can eject an electron that is only amplified by the subsequent
 263 stages, resulting in a lower measured charge (lower by a factor of approximately 10). For the
 264 IceCube PMTs, the prepulses have been found to arrive approximately 30 ns before the signal
 265 from other photoelectrons from the photocathode [6].

- 266 • **MPE contamination.** When multiple photoelectrons arrive at the first dynodes within several
 267 nanoseconds of each other, they can be reconstructed by the software as a single MPE pulse.

- 268 • **Dark noise.** Photoelectron emission, not initiated from an external event, can be attributed to
 269 thermionic emission from the low work function photocathode and the dynodes, Cherenkov
 270 radiations initiated from radioactive decay within the DOM, and field emission from the
 271 electrodes. It is shown in Fig. 28 of Ref. [18] that the dark noise preferentially populates the
 272 low-charge region.

- 273 • **Electronic noise.** This refers to the fluctuations in the analog-to-digital converters (ATWDs
 274 and FADC) and ringing that arises from the electronics.

275 Beyond the physical phenomena above that modify the measured charge distribution, there is
 276 also a lower limit on the smallest charge that can be extracted. For IceCube, the discriminator only
 277 triggers for peak voltages above the threshold and subsequent pulses in the readout time window
 278 are subject to a software-defined threshold. The software threshold was set conservatively to avoid
 279 extracting pulses that originated from electronic noise. This threshold can be modified to gain
 280 access to lower charge pulses and will be discussed in Sec. 2.2.

281 The standard SPE charge distribution used for all DOMs in IceCube, known as the TA0003
 282 distribution [6], models the above effects as the sum of an exponential plus a Gaussian. The TA0003
 283 distribution represents the average SPE charge distribution extracted from a lab measurement of
 284 118 Hamamatsu R7081-02 PMTs. This was performed in a -32°C freezer using a pulsed UV LED
 285 centered along the axis of the PMT, directly in front of the photocathode.

286 Recently, IceCube has made several lab measurements using the R7081-02 PMTs with in-time
 287 laser pulses, confirming that the in-time charge distribution includes a steeply falling low-charge
 288 component below the discriminator threshold. To account for this, a new functional form including
 289 a second exponential was introduced. This form of the charge distribution $f(q)_{\text{SPE}} = \text{Exp}_1 + \text{Exp}_2$
 290 + Gaussian, is referred to as the *SPE charge template* in this article. Explicitly, it is:

$$f(q)_{\text{SPE}} = E_1 e^{-q/w_1} + E_2 e^{-1/w_2} + N e^{-\frac{(q-\mu)^2}{2\sigma^2}}, \quad (1.1)$$

291 where q represents the measured charge; E_1 , E_2 , and N represent normalization factors of each
 292 component; w_1 and w_2 are the exponential decay widths; and μ , σ are the Gaussian mean and
 293 width, respectively. This is the assumed functional shape of the SPE charge distributions, and the
 294 components of Eq. 1.1 are determined in this article for all in-ice DOMs. IceCube defines 1 PE as
 295 the location of the Gaussian mean (μ) and calibrates the gain of the individual PMTs prior to the
 296 start of each season to meet this definition. The choice of where we define 1 PE is arbitrary, since
 297 linearity between the total charge collected and the number of incident photons is satisfied up to
 298 $\sim 2\text{ V}$ [7], or approximately 375 PE. This is because the average of the distribution is a set fraction
 299 of the Gaussian mean and the mean of a N -fold convolution is the sum of means. Any bias in the
 300 total observed charge can be absorbed into an efficiency term, such as the quantum efficiency.

301 1.2 IceCube datasets and software definitions

302 The amount of observed light depends on the local properties of the ice [19]. Short term climate
 303 variations from volcanoes and longer-term variations from atmospheric dust affect the optical
 304 properties of the ice, producing nearly horizontal layers. This layered structure affects how much
 305 light the DOMs see, and, with it, the trigger rate. The largest contribution to the IceCube trigger
 306 rate comes from downward-going muons produced in cosmic ray-induced showers [20]. Cosmic
 307 ray muons stopping in the detector cause the individual trigger rate to decrease at lower depths.

308 Thermionic emission induced dark noise is suppressed at lower temperatures. A study of the
 309 noise characteristics of the DOMs indicate that at the in-ice temperatures, the dominant source of
 310 dark noise originates from radioactive decay emanating from the spherical glass pressure vessel [7].

311 An induced signal in the PMT that passes through the AC coupling toroid located on the
 312 base of the PMT is compared to a discriminator threshold. If a DOM and its nearest or next-to-
 313 nearest neighbor observe a discriminator threshold crossing within a set time window, a *Hard Local*

314 *Coincidence* (HLC) is initiated, and the corresponding waveforms are sampled 128 times and read
315 out on the three ATWD channels. An HLC event is unlikely to originate from dark noise.

316 After waveform digitization, there is a correction applied to remove the measured DC baseline
317 offset. The signal droop and undershoot introduced by the toroidal transformer AC coupling is
318 compensated for in software during waveform calibration by adding the expected temperature-
319 dependent reaction voltage of the undershoot to the calibrated waveform. If the undershoot voltage
320 drops below 0 ADC counts, the ADC values are zeroed and then compensated for once the waveform
321 is above the minimum ADC input. For each version of the AC coupling, scaled single photoelectron
322 pulse shapes are then fit to the waveforms using software referred to as "WaveDeform" (waveform
323 unfolding process), which determines the individual pulse time stamps and charges and populates
324 a pulse series.

325 The pulse series used in this analysis come from two datasets provided by IceCube:

- 326 1. The **MinBias dataset**. This dataset records the full waveform readout of randomly-triggered
327 HLC events at a rate that corresponds on average to 1/1000 events. The largest contribution to
328 the IceCube trigger rate comes from downward-going muons produced in cosmic-ray-induced
329 showers [20] and therefore is the largest signal component in this dataset. These muons tend
330 to have small energies when they reach the detector, thus they produce minimal MPE con-
331 tamination. The full waveform of these events allows us to extract the raw information about
332 the individual pulses. This will be used to measure the individual PMT charge distributions.
- 333 2. The **BeaconLaunch dataset**. This is a forced triggered filter that is typically used to mon-
334 itor the individual DOM baseline. It includes the full ATWD-window waveform readout.
335 Since this dataset is forced-triggered, the majority of these waveforms represent DC baseline
336 fluctuations with minimal contamination from the occasional coincidental pulse that makes
337 it into the readout window. This dataset will be used to examine the noise contribution to the
338 charge distributions.

339 When using this dataset, the weight of every pulse is multiplied by a factor of 28.4 to account
340 for the livetime difference between the MinBias dataset and the BeaconLaunch dataset.
341 Weight, in this context, refers to the number of photons in the MinBias dataset proportional
342 to one photon in the BeaconLaunch dataset for which both datasets have the same equivalent
343 livetime.

344 This analysis uses the full MinBias and BeaconLaunch datasets from IceCube seasons 2011 to
345 2016 [21] (subsequently referred to as IC86.2011 to IC86.2016). Seasons in IceCube typically start
346 in May of the labeled year and end approximately one year later. Calibration is performed before
347 the start of each season.

348 **2 Extracting the SPE charge templates**

349 **2.1 Single photoelectron pulse selection**

350 The pulse selection is the method used to extract candidate, unbiased, single photoelectron pulses
351 from high-gain ATWD channel while minimizing the MPE contamination. It avoids collecting

352 afterpulses, rejects late pulses from the trigger, reassembles late pulses, accounts for the discrimi-
 353 nator threshold, reduces the effect of droop and baseline undershoot, and gives sufficient statistics
 354 to perform a season-to-season measurement. An illustrative diagram of the pulse selection is shown
 355 in the left side of Fig. 2, while a description of the procedure is detailed below.

356 We restrict the pulse selection to only extract information from waveforms in which the trigger
 357 pulse does not exceed 10 mV (~ 2 PE) and no subsequent part of the waveform exceeds 20 mV
 358 (~ 4 PE). This reduces the effect of the baseline undershoot due to the AC coupling or other artifacts
 359 from large pulses.

360 In order to trigger a DOM, the input to the front-end amplifiers must exceed the discriminator
 361 threshold. To avoid the selection bias of the discriminator trigger, we ignore the trigger pulse as well
 362 as the entire first 100 ns of the time window. Ignoring the first 100 ns has the added benefit of also
 363 removing late pulses that could be attributed to the triggering pulse. To ensure we are not accepting
 364 afterpulses into the selection, we also enforce the constraint that the pulse of interest (POI) is within
 365 the first 375 ns of the ATWD time window. This also allows us to examine the waveform up to
 366 50 ns after the POI. In the vicinity of the POI, we ensure that WaveDeform did not reconstruct any
 367 pulses up to 50 ns prior to the POI, or 100 to 150 ns after the POI (the light gray region of Fig. 2
 368 (left)). This latter constraint is to reduce the probability of accidentally splitting a late pulse in the
 369 summation window.

370 If a pulse is reconstructed between 100 and 375 ns after the start of the waveform and the voltage
 371 criteria are met, it is accepted as a candidate photoelectron and several checks are performed on
 372 the waveform prior to and after the pulse. The first check is to ensure that the waveform is near the

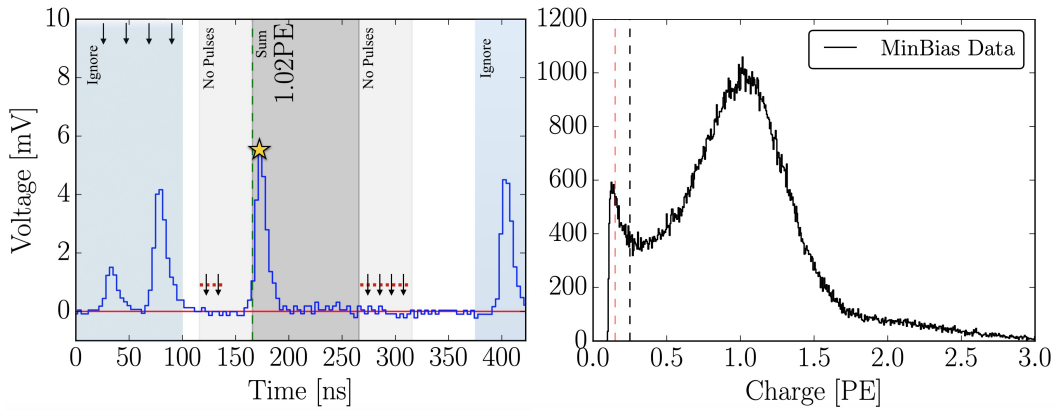


Figure 2. Left: An illustrative diagram of the pulse selection criteria for selecting a high-purity and unbiased sample of single photoelectrons. The digitized ATWD waveform is shown in blue. The pulse of interest is identified with a yellow star. This example waveform was triggered by a small pulse at 25 ns (recall that the delay board allows us to examine the waveform just prior to the trigger pulse), followed by a potential late pulse at 70 ns. At 400 ns, we see a pulse in the region susceptible to afterpulses. Waveform voltage checks are illustrated with arrows, and various time windows described in the text are drawn with semi-opaque regions. The POI is reported to have a charge of 1.02 PE, given by WaveDeform, and would pass the pulse selection criteria. Right: The collected charges from string 1, optical module 1 (DOM 1,1), from the MinBias dataset collected from IC86.2011 to IC86.2016 that pass the pulse selection. The discriminator threshold at 0.25 PE is represented as a dotted black vertical line. For visual purposes, a vertical dashed red line is also included at 0.15 PE.

373 baseline just before the rising edge of the POI. This is accomplished by ensuring that the waveform
 374 does not exceed 1 mV, 50 to 20 ns prior to the POI, and eliminates cases where the POI is a late
 375 pulse. We also ensure the waveform returns to the baseline by checking that no ADC measurement
 376 exceeds 1 mV, 100 to 150 ns after the POI. These constraints are illustrated as the horizontal red
 377 dotted lines and black arrows in the left side of Fig. 2.

378 If all the above criteria are met, we sum the reconstructed charges from the POI time, given by
 379 WaveDeform, to +100 ns (the dark gray area in Fig. 2 (left)). This ensures that any nearby pulses
 380 are either fully separated or fully added. WaveDeform may occasionally split an SPE pulse into
 381 multiple smaller pulses, therefore it is always critical to perform a summation of the charge within
 382 a window. The 100 ns summation also means that the pulse selection will occasionally accept MPE
 383 events.

384 2.2 Characterizing the low-charge region

385 Fig. 2 (right) shows the charge distributions of the selected pulses that pass the single photoelectron
 386 pulse selection for string 1, optical module 1, DOM(1,1). In the low-charge region (below 0.25 PE),
 387 we see a second threshold at approximately 0.13 PE. This is a software-defined threshold that comes
 388 from a gradient-related termination condition in WaveDeform. The threshold was set to avoid
 389 electronic noise being interpreted as PMT pulses and contaminating the low-charge region.

390 The steeply falling component of the region from 0.13 PE to 0.25 PE is in agreement with the
 391 in-time laser tests mentioned in Sec. 1.1 and emphasizes the importance of collecting data below the
 392 discriminator threshold. This section will assess the noise contribution to this region and examine
 393 the effect on the charge distribution and noise contribution by lowering the WaveDeform threshold.

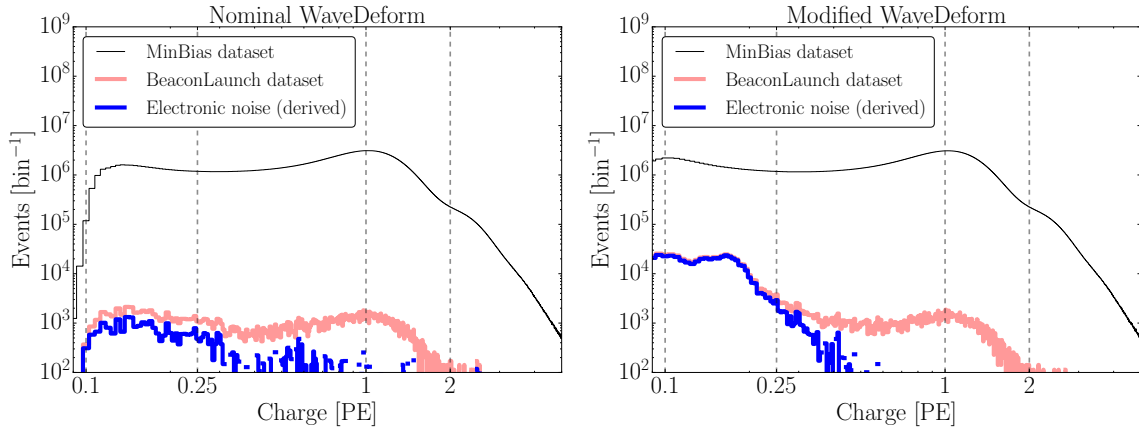


Figure 3. The cumulative charge distributions of all DOMs for the MinBias (M) and BeaconLaunch (B) datasets. The blue histogram shows the derived contribution from electronic noise. This was found by subtracting the normalized MinBias dataset from the BeaconLaunch dataset ($B - M \times (B|_{1PE}/M|_{1PE})$). Left: The charge distributions for the standard WaveDeform settings. Right: The charge distributions for the modified WaveDeform settings.

394 Fig. 3 (left) shows the charge distributions for the MinBias (black) and the BeaconLaunch

395 (red) datasets using the default settings of WaveDeform. As mentioned in Sec. 1.2, occasionally
 396 a photoelectron will be coincident with the forced BeaconLaunch time window. These charges
 397 populate a SPE charge distribution. Subtracting the shape of the MinBias charge distribution from
 398 the BeaconLaunch dataset yields an estimate of the amount of electronic noise contamination (blue).
 399 The bin with the lowest signal-to-noise ratio (SNR) above 0.1 PE was found to have a SNR of 744.7.
 400 The SNR for the full distribution was found to be 1.98×10^5 . Fig. 3 (right) shows the same data after
 401 lowering the WaveDeform threshold. Correspondingly, the bin with the lower SNR was found to
 402 have a SNR of 57.9, whereas the total SNR was found to be 0.69×10^5 .

403 The modified WaveDeform datasets show a minimal increase in the contribution of noise to
 404 the low-charge region. From this, we are able to extract charge information down to approximately
 405 0.10 PE and improve the overall description of the charge distribution below the discriminator. This
 406 will help constrain the values defining Exp_1 .

407 2.3 Fitting procedure

408 Fitting software is used to determine the components of Eq. 1.1 from the measured charge distri-
 409 bution that includes the MPE contamination. The fit assumes that there is a negligible three-PE
 410 contribution, which is justified by the lack of statistics in the 3 PE region as well as the significant
 411 rate difference between the 1 PE and 2 PE region, as shown in Fig. 2 (right). The 2 PE charge
 412 distribution is assumed to be the SPE charge distribution convolved with itself [22].

413 The exponential components of Eq. 1.1 represent poorly amplified photoelectrons, and we do
 414 not allow it to extend beyond the high-charge region of the Gaussian component. In particular, we
 415 include a constraint on the parameter w_2 to ensure that it falls off with the Gaussian component:

$$w_2 < \frac{\mu + 2\sigma}{4 - \ln(N/E_2)}. \quad (2.1)$$

416 This equation was found by setting the Exp_2 to be \exp^{-2} that of the Gaussian component at two
 417 sigma (the Exp_1 is neglected from this equation since it falls off in the low-charge region). Eq. 2.1
 418 is used as a constraint during the fit to the charge distributions.

419 Pulses that fall below the WaveDeform threshold and are not reconstructed contribute to an
 420 effective efficiency of the individual DOMs. This analysis assumes the same shape of the steeply
 421 falling exponential component (Exp_1) for all DOMs in the detector to avoid large fluctuations in
 422 the individual DOM efficiencies. The modified WaveDeform data will strictly be used to determine
 423 the Exp_1 component. Specifically, using the modified WaveDeform, we background-subtract the
 424 BeaconLaunch distribution from the MinBias data, fit the resulting distribution to determine the
 425 components of Eq. 2.1, and use only the measured shape and normalization of Exp_1 in all subsequent
 426 unmodified WaveDeform fits.

427 As described in Sec. 1.1, the Gaussian mean (μ) is used to determine the gain setting for each
 428 PMT. Therefore, it is particularly important that the fit quality in this region accurately describes the
 429 data. While fitting to the full charge distribution improves the overall fit agreement, the mismatch
 430 between the chosen functional form (Eq. 1.1) and a true SPE charge distribution can cause the
 431 Gaussian component to pull away from its ideal location. To compensate for this, the fitting
 432 algorithm prioritizes fitting to the data around the Gaussian mean. This is accomplished by first
 433 fitting to the full distribution to get an estimate of the Gaussian mean location. Then, the statistical

434 uncertainty is reduced in the region ± 0.15 PE around the original estimated Gaussian mean, and
 435 the distribution is re-fitted.

436 Upon fitting the MinBias data with the predetermined
 437 values for Exp_1 , the residual of each fit is calculated by
 438 measuring the percentage difference between the fit and
 439 the data. The average residual is then used as a global
 440 scaling factor for all SPE charge templates to account for
 441 the difference between the chosen model (Eq. 2.1) and
 442 the actual data.

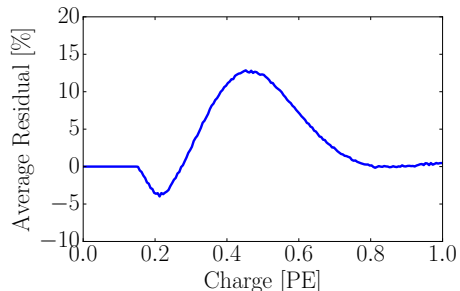


Figure 4. The measured average residual of the SPE charge templates fit.

443 2.4 SPE charge template fit results

444 Using the background-subtracted modified WaveDeform
 445 dataset, the Exp_1 component was determined by fitting
 446 the distribution from 0.1 PE to 3.5 PE. The result of the
 447 fit yielded $E_1 = 6.9 \pm 1.5$ and $w_1 = 0.032 \pm 0.002$ PE. The
 448 shape of Exp_1 is then used to describe the low-PE charge
 449 region for all subsequent fits.

450 Using the MinBias dataset with the measured values of Exp_1 , the SPE charge templates are
 451 extracted for every DOM, separately for each IceCube season from IC86.2011 to IC86.2016. The
 452 fit range for Exp_2 and the Gaussian components is selected to be between 0.15 PE and 3.5 PE. An
 453 average fit was also performed on the cumulative charge distribution, in which all the data for a
 454 given DOM was summed together (labeled as "AVG").

455 All the DOMs with "failed fits" are not included in this analysis. A DOM is classified as having
 456 a failed fit if it does not pass one of the validity checks on the data requirements (e.g. the number of
 457 valid pulses) or goodness of fit. The majority of these DOMs have been removed from service (107
 458 to 111 DOMs over the seasons considered), and the remaining 6 DOMs that failed the AVG fits are
 459 known to have various issues. In the IceCube MC simulation chain, these DOMs are assigned the
 460 average SPE charge template.

461 We can divide the DOMs into subset of hardware differences: the HQE DOMs with the new
 462 toroids, the Standard QE DOMs with the new toroids, and the Standard QE DOMs with the old
 463 toroids. The mean value and standard error of the IC86.AVG fit parameters, excluding Exp_1 , for
 464 the subset of hardware differences are listed in Table 1. The average residual for all DOMs from 0
 465 to 1 PE is shown in Fig. 4.

| Hardware Configuration | Exp_2 Amp. (E_2) | Exp_2 Width (w_2) | Gaus. Amp. (N) | Gaus. Mean (μ) | Gaus. Width (σ) |
|------------------------|-------------------------------|--------------------------------|-------------------|----------------------|--------------------------|
| HQE / New Toroid | 0.644 ± 0.003 | 0.405 ± 0.003 | 0.715 ± 0.002 | 1.0202 ± 0.0010 | 0.311 ± 0.001 |
| Std. QE / New Toroids | 0.566 ± 0.001 | 0.403 ± 0.001 | 0.751 ± 0.001 | 1.0238 ± 0.0004 | 0.316 ± 0.001 |
| Std. QE / Old Toroids | 0.525 ± 0.002 | 0.420 ± 0.002 | 0.813 ± 0.002 | 1.0074 ± 0.0007 | 0.294 ± 0.001 |

Table 1. The average values and standard error of each fit parameter for the subset of hardware configurations listed in the first column.

466 An example fit is shown in Fig. 5 for the cumulative MinBias charge distribution for DOM
 467 (1,1). The collected charge distribution is shown in the black histogram, while the fit to the data is

468 shown as the black line. The extracted SPE charge template from the fit is shown in blue. Both the
 469 fit and extracted SPE charge template have been scaled by the average residual shown in Fig. 4.

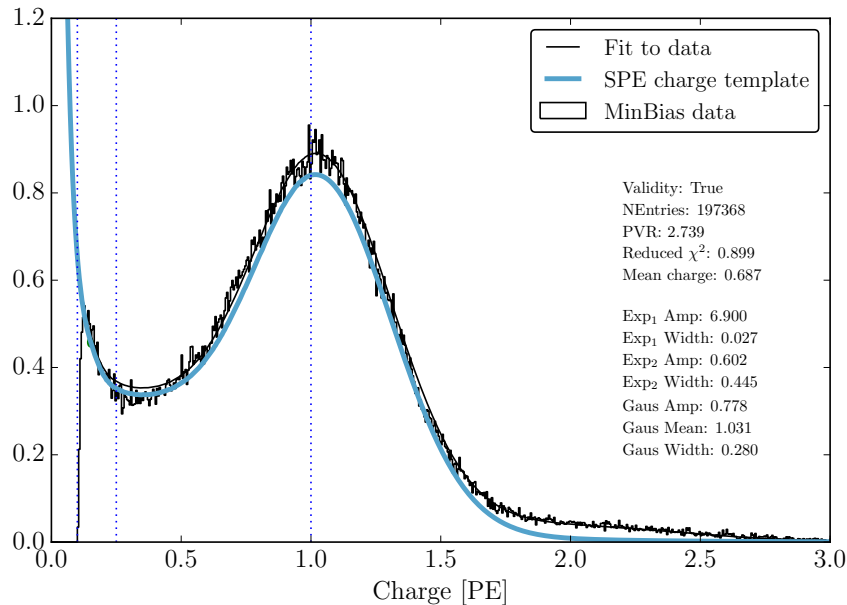


Figure 5. An example fit for DOM(1,1) using the MinBias dataset including data from seasons IC86.2011 to IC86.2016. The result of the fit is shown as a solid black line and the extracted SPE charge template from the fit is shown in blue. For both the fit and the SPE charge template, the curves include the correction from the average residual shown in Fig. 4.

470 3 Discussion

471 3.1 Correlations between fit parameters and DOM hardware differences

472 It is evident from the data in Table 1 that the average shape of the SPE charge templates is correlated
 473 with the DOM hardware. These differences can also be seen in the measured peak-to-valley ratios
 474 and mean charge of the SPE charge template (see Fig. 6). When we examine the subset of DOMs
 475 instrumented with the new toroids, the average HQE DOM were found to have a $13.8 \pm 0.6\%$ larger
 476 E_2 component and $4.77 \pm 0.03\%$ smaller Gaussian amplitude. Consequently, the average HQE
 477 peak-to-valley ratio is measured to be 2.322 ± 0.013 , corresponding to $12.12 \pm 0.06\%$ lower than
 478 the average Standard QE DOMs. Also, interestingly, the mean charge of the average HQE DOM
 479 was found to be $3.34 \pm 0.01\%$ lower than that of the Standard QE DOMs. IceCube compensates for
 480 the change in the mean measured charge in simulation, by increasing the HQE DOM efficiency by
 481 the equivalent amount. This ensures that the total amount of charge collected by the HQE DOMs
 482 remains the same prior to, and after, inserting the SPE charge templates into simulation.

483 Similarly, using only the subset of Standard QE DOMs, the SPE charge templates compar-
 484 ing the method of AC coupling were found to have measurably different shapes. The average
 485 Gaussian amplitude and width for the DOMs instrumented with the old toroids were found to be

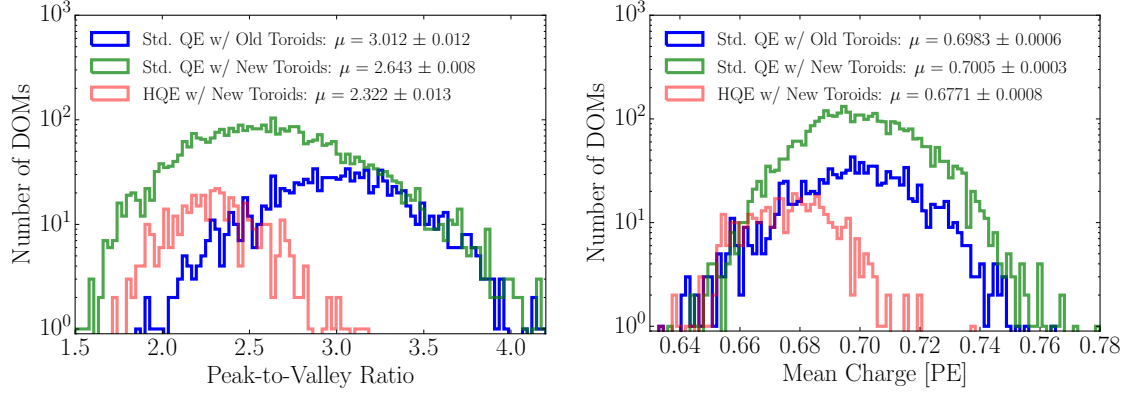


Figure 6. Comparison between the R7081-02MOD HQE DOMs and standard R7081-02 DOMs. Left: The peak-to-valley ratio for the two subsets of quantum efficiencies. Right: The mean charge of the individual DOM SPE charge templates.

486 $8.31 \pm 0.01\%$ and $-6.80 \pm 0.03\%$, respectively. With these differences, we find a peak-to-valley
 487 ratio of 2.643 ± 0.008 for the new toroid DOMs and 3.012 ± 0.012 for the old toroid DOMs. The
 488 average Gaussian mean of the fit for the DOMs with the old toroids was also found to be $1.6 \pm 0.1\%$
 489 lower than those with the new toroids. This corresponds proportionally to a change in the expected
 490 gain. The mean charge, however, between these two hardware configurations remains very similar
 491 ($-0.346 \pm 0.001\%$).

492 Although the DOMs instrumented with the old toroids were deployed into the ice earlier than
 493 those with the new toroids, the differences above is still noted when examining individual deployment
 494 years; therefore, the shape differences are not attributed to the change in the DOM behavior over time.
 495 However, the DOMs with the old toroids were the first PMTs to be manufactured by Hamamatsu.
 496 A gradual change over time of the fit parameters was observed when ordering the PMTs according
 497 to their PMT serial number. This is compelling evidence that the observed differences between
 498 the new and old toroids is due to a change in the production procedure rather than version of AC
 499 coupling.

500 Fig. 7 illustrates the average shape differences in the extracted SPE charge templates between
 501 the HQE DOM with the new toroids (solid white line), Standard QE with the new toroids (dotted
 502 white line), Standard QE with the old toroids (dashed white line), compared to the spread in the
 503 measured SPE charge templates for all DOMs in the detector (dark blue contours). The figure
 504 also shows how the TA0003 distribution compares to this recent measurement. The observable
 505 shape differences from the TA0003 are attributed to a better control of the low-charge region, the
 506 difference in functional form (described in Section 1.1), and the fact that the SPE charge templates
 507 were generated using a realistic photocathode illumination.

508 3.2 Fitting parameters variation over time

509 The SPE charge templates were extracted for each IceCube season independently to investigate the
 510 time dependence of the fit parameters. For every DOM in the detector, the change over time of each
 511 fit parameter (excluding Exp_1) was calculated. Fig. 8 shows the change in a given fit parameter,
 512 relative to the mean value, per year. The measured distribution was found to be consistent with

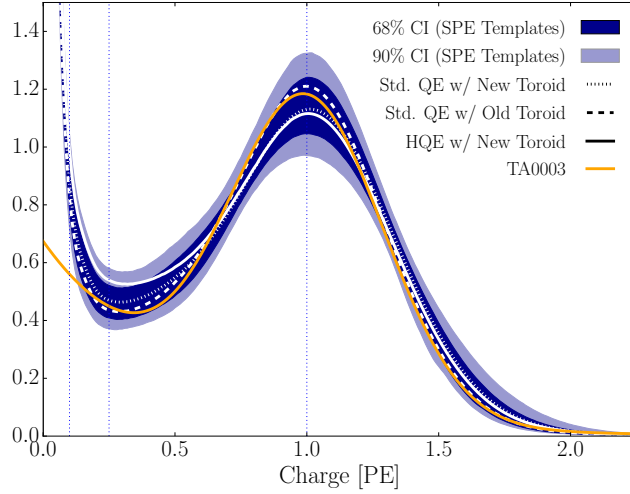


Figure 7. The inner (outer) dark blue region shows the 68% (90%) confidence interval defined by the measured spread in the extracted SPE charge templates of all DOMs in the detector. Superimposed, is the average SPE charge template for the variety of hardware configurations shown in white. The TA0003 distribution is shown in orange. All curves have been normalized such that the area above 0.25 PE is the same.

513 statistically scrambling the yearly measurements. The average of each fit parameters are found to
 514 deviate less than 0.1%, which is in agreement with the stability checks performed in Ref. [7]. This
 515 observation holds for the individual subset of DOMs with different hardware configurations as well.

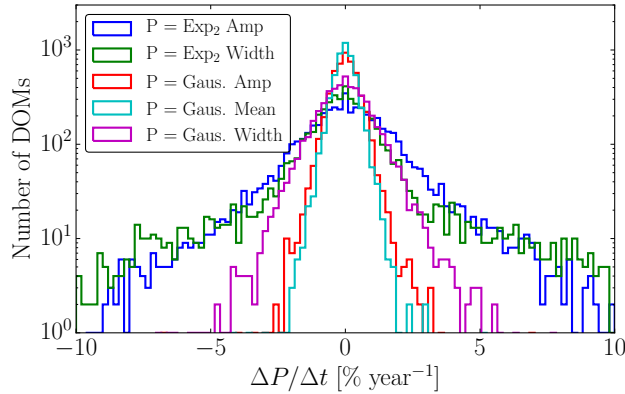


Figure 8. The change in the individual DOM fitted parameters over time, represented as percentage deviation from the mean fit parameter value.

516 3.3 Quantifying observable changes when modifying the PMT charge distributions

517 Changing the assumed gain response in simulation, as deduced from data, has different implications
 518 depending on the typical illumination level present in different analyses. These differences are

519 outlined in the following discussion.

520 The PMT response is described by a combination of a "bare" efficiency, η_0 , and a normalized
 521 charge response function, $f(q)$. The bare efficiency represents the fraction of arriving photons that
 522 result in any nonzero charge response, including those well below the discriminator threshold. The
 523 normalization condition is:

$$\int_0^{\text{inf}} f(q) dq = 1. \quad (3.1)$$

524 Generally, $f(q)$ and η_0 have to be adjusted together to maintain agreement with a quantity known
 525 from lab or in-ice measurements, such as the predicted number of pulses above threshold for a dim
 526 source.

527 **Dim source measurements** Where light levels are low enough, low occupancy ensures that
 528 sub-discriminator pulses do not contribute any observed charge as they do not satisfy the trigger
 529 threshold. Given some independent way of knowing the number of arriving photons, a lab or in-ice
 530 measurement determines the trigger fraction above threshold $\eta_{0.25}$ and/or the average charge over
 531 threshold $Q_{0.25}$, either of which can be used to constrain the model as follows:

$$\eta_{0.25} = \eta_0 \int_{0.25q_{pk}}^{\infty} f(q) dq \quad (3.2)$$

$$Q_{0.25} = \eta_0 \int_{0.25q_{pk}}^{\infty} q f(q) dq \quad (3.3)$$

532 Here, the discriminator threshold is assumed to be 0.25 times the peak position q_{pk} . It is also
 533 useful to multiply observed charges by q_{pk} , since we set each PMT gain by such a reference, and
 534 then a measurement constraint would be stated in terms of $Q_{0.25}/q_{pk}$.

535 **Semi-bright source measurements** Once the ATWD window is open, subsequent pulses are not
 536 limited by the discriminator threshold. WaveDeform introduces a software termination condition at
 537 0.1 PE (described at the end of Section 2.1). The average charge of an individual pulse that arrives
 538 within the time window is:

$$Q_{0.10} = \eta_0 \int_{0.10q_{pk}}^{\infty} q f(q) dq \quad (3.4)$$

539 **Bright source measurements** For light levels that are large, the trigger is satisfied regardless
 540 of the response to individual photons, and the total charge per arriving photon therefore includes
 541 contributions below both the discriminator and the WaveDeform thresholds:

$$Q_0 = \eta_0 \int_0^{\infty} q f(q) dq \quad (3.5)$$

542 As such, the total charge is directly proportional to the average charge of the SPE charge
 543 template, having a strong dependence on Exp_1 .

| Model | Detector | $Q_0/Q_{0.25}$ | $Q_0/Q_{0.10}$ | $\eta_{0.25}/Q_{0.25}$ |
|----------------------|-----------------------|-------------------|---------------------|------------------------|
| TA0003 | All DOMs | 1.017 | 1.0031 | 1.05 |
| SPE charge templates | HQE + New Toroids | 1.021 ± 0.002 | 1.0041 ± 0.0004 | 1.05 ± 0.02 |
| | Std. QE + New Toroids | 1.018 ± 0.002 | 1.0035 ± 0.0005 | 1.03 ± 0.02 |
| | Std. QE + Old Toroids | 1.017 ± 0.002 | 1.0033 ± 0.0005 | 1.05 ± 0.02 |

Table 2. The distribution in bright-to-dim ratios for the previous charge distribution (TA0003) and the individual DOM SPE charge templates for the IceCube and DeepCore detectors.

544 3.3.1 Model comparison

545 When the charge distribution model is changed in a way that preserves agreement with the measured
546 $\eta_{0.25}$ or $Q_{0.25}/q_{pk}$, i.e. η_0 is adjusted properly for changes in $f(q)$, the physical effect can be
547 summarized by the change in the bright-to-dim ratios $Q_0/Q_{0.25}$, and $Q_0/Q_{0.10}$. Conveniently, these
548 ratios depend only on the shape of $f(q)$. Table 2 compares these ratios in terms of the TA0003 charge
549 distribution and the SPE charge templates described here. It is shown that there are sub-percent
550 level differences in the physically-observable bright-to-dim ratios.

551 3.4 SPE charge templates for calibration

552 The gain setting on each PMT is calibrated prior to the beginning of each season such that the
553 Gaussian mean of the charge distribution corresponds to a gain of 10^7 , or equivalently 1 PE.
554 This gain calibration method, run directly on the DOMs, uses waveform integration for charge
555 determination instead of WaveDeform unfolding, resulting in a small systematic shift in gain. This
556 systematic shift was determined for every PMT, and was found to be on average $2.00 \pm 0.03\%$ with
557 a standard deviation of 3.54% , corresponding to an overestimation of the measured charge in the
558 detector.

559 The correction to the systematic shift in the measured charge can be implemented retroactively
560 by dividing the reported charge from WaveDeform by the corresponding offset for a given DOM.
561 Alternatively, we can account for this by simply inserting SPE charge templates, measured in this
562 analysis, into simulation such that the corresponding systematic shift is also modelled in simulation.
563 This will be performed in the following subsection.

564 3.5 SPE charge templates in simulation

565 The IceCube MC simulation chain assigns a charge to every photoelectron generated at the surface
566 of the photocathode. The charge is determined by sampling from a normalized charge distribution
567 probability density function. A comparison between describing the charge distribution using the
568 SPE charge templates and the TA0003 distribution follows.

569 Two simulation sets consisting of the same events were processed through the IceCube Monte
570 Carlo simulation chain to the final analysis level of an update to the IC86.2011 sterile neutrino analy-
571 sis [23]. Here, the events that pass the cuts are $>99.9\%$ upward-going (a trajectory oriented upwards
572 relative to the horizon) secondary muons produced by charged current muon neutrino/antineutrino
573 interactions. The muon energy range of this event selection is between approximately 500 GeV and
574 10 TeV.

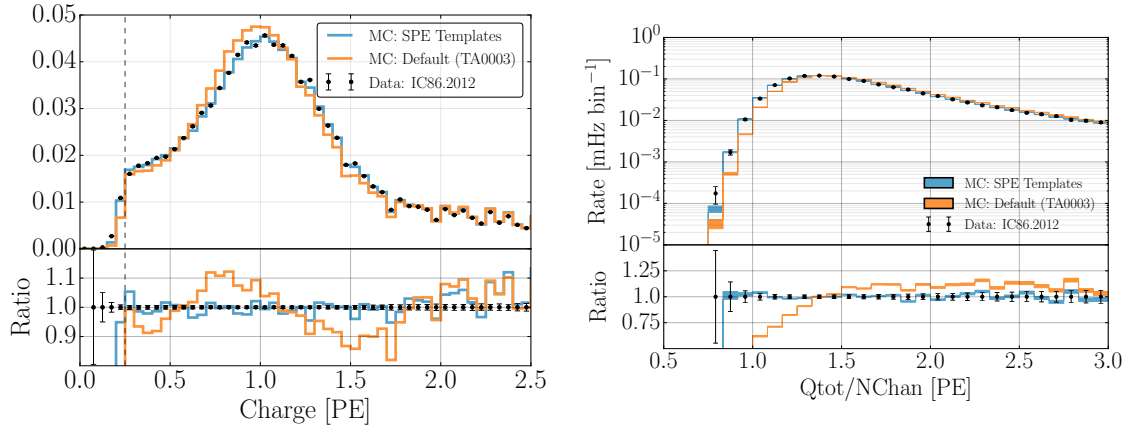


Figure 9. A comparison between the SPE charge templates (blue) and the TA0003 (orange) model for describing the SPE charge distribution in Monte Carlo. The simulation is compared to the 2012 IceCube season. Left: The total measured charge per DOM, per event at analysis level. Right: The distribution of the total measured charge of an event divided by the number of DOMs that participated in the event.

575 Fig. 9 (left) shows the distribution of the total measured charge in a single DOM during an
 576 event. The data is shown for the full IC86.2012 season but is statistically equivalent to any of the
 577 other seasons. The simulation set using the TA0003 charge distribution is shown in orange, and
 578 that using the SPE charge templates is shown in blue. Fig. 9 (right) shows the distribution of the
 579 measured total charge of an event divided by the number of channels (NChan), or DOMs, that
 580 participated in the event. Both plots in Fig. 9 have been normalized such that the area under the
 581 histograms is the same.

582 The SPE charge templates clearly improve the overall MC description of these two low-level
 583 variables. This update may be useful for analyses that rely on low-occupancy events (low-energy or
 584 dim events) in which average charge per channels is below 1.5 PE, and will be investigated further
 585 within IceCube.

586 4 Conclusion

587 This article outlines the procedure used to extract the SPE charge templates for all in-ice DOMs in the
 588 IceCube detector using in-situ data from IC86.2011 to IC86.2016. The result of this measurement
 589 was shown to be useful for improving the overall data/MC agreement as well as calibration of the
 590 individual PMTs. It also prompted a comparison between the shape of the SPE charge templates
 591 for a variety of hardware configurations and time dependent correlations.

592 The subset of HQE DOMs were found to have a smaller peak-to-valley ratio relative to the
 593 Standard QE DOMs, as well as an overall $3.34 \pm 0.01\%$ lower mean charge. It was also found that the
 594 DOMs instrumented with the old toroids used for AC coupling (the first PMTs to be manufactured)
 595 had narrower and larger Gaussian component corresponding resulting in an increased peak-to-valley
 596 ratio of $14.0 \pm 0.6\%$. No significant time dependence in any of the fitted parameters associated with
 597 the SPE charge templates over the investigated seasons was observed. A reassessment of the PMT
 598 gain settings found a systematic bias of $2.00 \pm 0.03\%$ with a standard deviation of 3.54% .

599 The SPE charge templates were inserted into the MC simulation and the results were compared
600 to the default TA0003 distribution. A significant improvement in the description of the low-level
601 variables, total charge per DOM and total charge over the number of channels, was shown. Analyses
602 which rely on low-light occupancy measurements, may benefit from this update. As shown in the
603 bright-to-dim ratios, the average mean charge for various light levels will not be affected by this
604 update.

605 **Acknowledgments**

606 We acknowledge the support from the following agencies:

607 USA – U.S. National Science Foundation-Office of Polar Programs, U.S. National Science
608 Foundation-Physics Division, Wisconsin Alumni Research Foundation, Center for High Throughput
609 Computing (CHTC) at the University of Wisconsin-Madison, Open Science Grid (OSG), Extreme
610 Science and Engineering Discovery Environment (XSEDE), U.S. Department of Energy-National
611 Energy Research Scientific Computing Center, Particle astrophysics research computing center at
612 the University of Maryland, Institute for Cyber-Enabled Research at Michigan State University, and
613 Astroparticle physics computational facility at Marquette University; Belgium – Funds for Scien-
614 tific Research (FRS-FNRS and FWO), FWO Odysseus and Big Science programmes, and Belgian
615 Federal Science Policy Office (Belspo); Germany – Bundesministerium für Bildung und Forschung
616 (BMBF), Deutsche Forschungsgemeinschaft (DFG), Helmholtz Alliance for Astroparticle Physics
617 (HAP), Initiative and Networking Fund of the Helmholtz Association, Deutsches Elektronen Syn-
618 chrotron (DESY), and High Performance Computing cluster of the RWTH Aachen; Sweden –
619 Swedish Research Council, Swedish Polar Research Secretariat, Swedish National Infrastructure
620 for Computing (SNIC), and Knut and Alice Wallenberg Foundation; Australia – Australian Re-
621 search Council; Canada – Natural Sciences and Engineering Research Council of Canada, Calcul
622 Québec, Compute Ontario, Canada Foundation for Innovation, WestGrid, and Compute Canada;
623 Denmark – Villum Fonden, Danish National Research Foundation (DNRF), Carlsberg Foundation;
624 New Zealand – Marsden Fund; Japan – Japan Society for Promotion of Science (JSPS) and Institute
625 for Global Prominent Research (IGPR) of Chiba University; Korea – National Research Foundation
626 of Korea (NRF); Switzerland – Swiss National Science Foundation (SNSF); United Kingdom –
627 Department of Physics, University of Oxford.

628 References

- 629 [1] J. Ahrens et al., *IceCube preliminary design document*, URL:
630 <https://icecube.wisc.edu/icecube/static/reports/IceCubeDesignDoc.pdf> (2001) .
- 631 [2] A. Achterberg et al., *First year performance of the IceCube neutrino telescope*, *Astroparticle Physics*
632 **26** (2006) 155–173, [[arXiv:astro-ph/0604450v2](https://arxiv.org/abs/astro-ph/0604450v2)].
- 633 [3] M. G. Aartsen et al., *Evidence for high-energy extraterrestrial neutrinos at the IceCube detector*,
634 *Science* **342** (2013) 1242856, [[arXiv:1311.5238v2](https://arxiv.org/abs/1311.5238v2)].
- 635 [4] R. Abbasi et al., *The design and performance of IceCube DeepCore*, *Astroparticle physics* **35** (2012)
636 615–624, [[arXiv:1109.6096v1](https://arxiv.org/abs/1109.6096v1)].
- 637 [5] R. Abbasi et al., *The IceCube data acquisition system: Signal capture, digitization, and timestamping*,
638 *NIM-A* **601** (2009) 294–316, [[arXiv:0810.4930v2](https://arxiv.org/abs/0810.4930v2)].
- 639 [6] R. Abbasi et al., *Calibration and characterization of the IceCube photomultiplier tube*, *NIM-A* **618**
640 (2010) 139–152, [[arXiv:1002.2442v1](https://arxiv.org/abs/1002.2442v1)].
- 641 [7] M. G. Aartsen et al., *The IceCube Neutrino Observatory: Instrumentation and Online Systems*, *JINST*
642 **12** (2017) 1748–0221, [[arXiv:1612.05093v2](https://arxiv.org/abs/1612.05093v2)].
- 643 [8] M. Aartsen et al., *Energy reconstruction methods in the IceCube Neutrino Telescope*, *JINST* **9** (2014)
644 1748–0221, [[arXiv:1311.4767v3](https://arxiv.org/abs/1311.4767v3)].
- 645 [9] R. Stokstad, *Design and performance of the IceCube electronics*,
646 URL: <https://cds.cern.ch/record/920022/files/p20.pdf> (2005) .
- 647 [10] Hamamatsu, *Resources: Basics and Applications*,
648 URL: https://www.hamamatsu.com/resources/pdf/etd/PMT_handbook_v3aE.pdf (2018) .
- 649 [11] Hamamatsu, *Handbook Resources, Chapter 4*, URL: https://www.hamamatsu.com/resources/pdf/etd/PMT_handbook_v3aE-Chapter4.pdf (2018) .
- 650 [12] J. Brack et al., *Characterization of the Hamamatsu R11780 12 in. photomultiplier tube*, *NIM-A* **712**
651 (2013) 162–173, [[arXiv:1210.2765v2](https://arxiv.org/abs/1210.2765v2)].
- 652 [13] E. Calvo et al., *Characterization of large-area photomultipliers under low magnetic fields: Design*
653 *and performance of the magnetic shielding for the Double Chooz neutrino experiment*, *NIM-A* **621**
654 (2010) 222–230, [[arXiv:0905.3246v1](https://arxiv.org/abs/0905.3246v1)].
- 655 [14] F. Kaether and C. Langbrandtner, *Transit time and charge correlations of single photoelectron events*
656 *in R7081 photomultiplier tubes*, *JINST* **7** (2012) P09002, [[arXiv:1207.0378v2](https://arxiv.org/abs/1207.0378v2)].
- 657 [15] B. Lubsandorzhev, P. Pokhil, R. Vasiljev and A. Wright, *Studies of prepulses and late pulses in the 8"*
658 *electron tubes series of photomultipliers*, *NIM-A* **442** (2000) 452–458.
- 659 [16] K. Ma et al., *Time and amplitude of afterpulse measured with a large size photomultiplier tube*,
660 *NIM-A* **629** (2011) 93–100, [[arXiv:0911.5336v1](https://arxiv.org/abs/0911.5336v1)].
- 661 [17] S. Torre, T. Antonioli and P. Benetti, *Study of afterpulse effects in photomultipliers*, *Review of*
662 *scientific instruments* **54** (1983) 1777–1780.
- 663 [18] Hamamatsu, *Photomultiplier tubes: Construction and Operating Characteristics*,
664 URL: https://www.hamamatsu.com/resources/pdf/etd/PMT_TPMZ0002E.pdf (2016) .
- 665 [19] M. Aartsen et al., *Measurement of South Pole ice transparency with the IceCube LED calibration*
666 *system*, *NIM-A* **711** (2013) 73–89, [[arXiv:1301.5361v1](https://arxiv.org/abs/1301.5361v1)].
667

- 668 [20] M. Aartsen et al., *Characterization of the atmospheric muon flux in IceCube*, *Astroparticle physics* **78**
669 (2016) 1–27, [[arXiv:1506.07981v2](#)].
- 670 [21] M. Aartsen et al., *Search for steady point-like sources in the astrophysical muon neutrino flux with 8*
671 *years of IceCube data*, *The European Physical Journal C* **79** (2019) 234, [[arXiv:1811.07979v2](#)].
- 672 [22] R. Dossi, A. Ianni, G. Ranucci and O. J. Smirnov, *Methods for precise photoelectron counting with*
673 *photomultipliers*, *NIM-A* **451** (2000) 623–637.
- 674 [23] M. Aartsen et al., *Searches for sterile neutrinos with the IceCube detector*, *Physical review letters* **117**
675 (2016) 071801, [[arXiv:1605.01990v2](#)].